ELSEVIER

Journal of Quantitative Spectroscopy & Radiative Transfer 102 (2006) 25–36

Journal of Quantitative Spectroscopy & Radiative Transfer

www.elsevier.com/locate/jqsrt

Effect of detailed cell structure on light scattering distribution: FDTD study of a B-cell with 3D structure constructed from confocal images

R. Scott Brock[a], Xin-Hua Hu[a], Douglas A. Weidner[b], Judith R. Mourant[c], Jun Q. Lu[a,*]

[a]*Department of Physics, East Carolina University, Greenville, NC 27858, USA*
[b]*Department of Microbiology and Immunology, Brody School of Medicine, East Carolina University, Greenville, NC 27858, USA*
[c]*Los Alamos National Laboratory, Bioscience Division, Los Alamos, NM 87545, USA*

Abstract

Human B-cells play an important role in the immune system, and because of their relatively simple structures with a nearly spherically shaped cell membrane and a large nucleus, they provide a good case to study on how the details of cell structure affect light scattering properties. A finite-difference-time-domain (FDTD) method is used to calculate angle-resolved light scattering distributions from a B-cell. Published FDTD simulations to date have used a smooth shape with a certain degree of symmetry to approximate the actual cell shape. In contrast, for this work, the shapes of the cell and its nucleus were determined from confocal microscopy measurements. An automated procedure was developed to construct a realistic three-dimensional structure of a B-cell from a stack of two-dimensional confocal images. The angle-resolved Mueller matrix elements of the B-cell were calculated and averaged for 30 different angles of incidence using a parallel FDTD code. These results were compared with those from a homogeneous and a coated sphere. Scattering from the two sphere models and the B-cell were very similar for scattering angles less than 5°, and the coated sphere and B-cell agreed well for scattering angles up to 20°. However, at larger angles, the scattering from the B-cell was a much smoother function of angle than scattering from either sphere model. Additionally, the homogeneous sphere results were the most similar to the B-cell results for most angles between 120° and 150°, and at angles greater than 150°, the B-cell scattered more light than either of the spheres. These results yield strong evidence that accurate modeling of light scattering by biological cells requires not only the high accuracy of the employed numerical method but the realistic cellular structure as input information as well.
© 2006 Elsevier Ltd. All rights reserved.

Keywords: Cell scattering; B-cell; FDTD; 3D cell structure; Confocal construction

1. Introduction

Elastic light scattering is one of the most probable pathways through which biological cells interact with optical radiation in the spectral regions of visible and infrared. The rich structure in the scattered light

*Corresponding author. Fax: +1 252 328 6314.
E-mail address: luj@ecu.edu (J.Q. Lu).

0022-4073/$ - see front matter © 2006 Elsevier Ltd. All rights reserved.
doi:10.1016/j.jqsrt.2006.02.075

distributions has been shown to yield abundant information on the cellular morphology due to the large size parameters and significant optical heterogeneity of biological cells [1–6]. As a result, light scattering is expected to provide an exquisitely sensitive approach for fast and non-invasive determination of cellular morphology and consequent cell sorting. A prominent example of its applications can be found in the development of flow cytometry for cell discrimination on the basis of light scattering signals [7,8]. Fulfilling the potential of flow cytometry as a powerful technique of cell analysis and diagnosis in cell biology and clinics requires continuous improvement in instrumentation, and development of accurate and efficient modeling tools. Light scattering by a biological cell is a complex phenomenon, since in general cells are dielectric bodies with an inhomogeneous spatial distribution in their refractive index and have shapes far from simple forms such as spheres or spheroids. In these cases, numerical methods have to be used, and the finite-difference-time-domain (FDTD) method is often adopted for this purpose [9]. In addition to a suitable numerical modeling method, proper optical structure and shape model are also necessary to ensure the accuracy of simulation results. In previous studies of cell scattering, the shapes of cell and nucleus were often modeled as ellipsoids [9,10] where the axial lengths were determined from the overall shape feature of the cell or nucleus. Recently, we have reported the development of an FDTD code and its parallel version to numerically model light scattering distributions by single red blood cells in different biconcave and deformed shapes [11,12]. Our results show that the shape of the scatterer can significantly affect the scattering patterns of a cell. While the shapes of red blood cells in these studies are based on the microscopic measurements of their morphology under different physiological and mechanical conditions, the shapes nevertheless were generated with analytical functions of rotational symmetry and with no consideration of detailed surface structures or slight deformation from the rotational symmetry. In this report, we present an automated procedure to construct the three-dimensional (3D) structure of a cultured B-lymphocyte, or B-cell, from a stack of 2D confocal images. The light scattering patterns of a B-cell with its reconstructed structure were calculated using a parallel FDTD code [12]. To understand to what extent that realistic shape and structure of a cell will affect its light scattering pattern. The results obtained from the constructed B-cell structure were compared with those obtained from an equivalent homogeneous sphere and a coated sphere with equal volume partition. We start in the next section with a description of the image construction procedure followed by the presentation of the FDTD simulation results and discussion.

2. Method

B-cells constitute 10–20% of the lymphocyte population, with the others being the T-cells, in human blood as a principal cellular component of the adaptive immune response. The morphological and behavioral spectra of B-cells are remarkable; partly because they derive from diverse normal lymphoid cells. The B-cells differentiate to form antibody-secreting plasma cells in tissue with enlarged cell volumes and play an important role in the understanding and diagnosis of lymphomas and leukemia. Inactive B-cells in blood have a slightly elongated shape with diameters ranging from 6 to 9 μm and nuclei occupying a large portion of the cell volume with diameters from 5 to 8 μm [13]. The cytoplasm forms a narrow rim with a considerable number of free ribosomes and a minimal rough endoplasmic reticulum. Activated B-cells, en route to form plasma cells, have increased sizes ranging from 9 to 15 μm due mainly to a greater amount of cytoplasm.

To simulate light scattering by a single B-cell using the FDTD method, the 3D optical structure of the cell is needed. In the FDTD method, the linear response of the biological cell to the incident light field is described by a spatially variant dielectric constant $\varepsilon(\mathbf{r})$, and the simulated region that includes the scatterer and its nearby region is discretized into rectangular grid cells with the corresponding values of $\varepsilon(\mathbf{r})$ assigned over the grid [14,15]. For biological cells of multiple intracellular components, it is necessary to define the boundary of each cell component so that the grid points within the boundary of a cellular component can be associated with the correct value of the dielectric constant. This requires accurate mapping of the 3D structure of the cell into the FDTD code. Confocal microscopy is a powerful tool to generate the 3D structure of a cell. A stack of 2D confocal images can be acquired with very small focal depth as the imaged cell is being translated along the z-axis, from which the 3D structure of the cell can be constructed. The z-axis is defined to be perpendicular to the focal plane of the microscope objective. In the subsections below, we describe a procedure that automatically constructs the 3D structure of a B-cell using a stack of 2D confocal images.

2.1. Confocal microscopy

Cultured NALM-6 cells, a human B-cell precursor derived from the peripheral blood of a patient with acute lymphoblastic leukemia [16], were used in our study. For confocal imaging, freshly harvested NALM-6 cells were simultaneously stained with two fluorescent dyes for 3 h at 37 °C to optimize the image contrast of different cellular components: the FM 1-43 dye [*N*-(3-triethylammoniumpropyl)-4-(4-(dibutylamino) styryl)pyridinium dibromide] at a concentration of 4 μM for membranes and the SYTO 61 Red dye at a concentration of 5 μM for the nucleus. Excess dye was then washed away to reduce background noise in the confocal images of the cells. The stained cells were placed on a glass depression slide to minimize cell distortion by the cover glass, and imaged with a laser scanning confocal microscope (LSM 510, Zeiss) using a 63 × water immersion objective to produce an image stack along the *z*-axis. Two laser beams at the wavelengths of 488 and 633 nm were used to excite the two dyes with the green fluorescence from the FM 1-43 and the red fluorescence from the SYTO 61. The two fluorescent light signals were acquired separately by two photomultipliers with appropriate filters. The combined fluorescence images were saved in a RGB image file stack with 512 × 512 pixels of 0.04 pixel distance at the focal plane in each 2D image, and the step size of the *z*-scan was set at 0.51 μm.

Image stacks of several NALM-6 cells were obtained, and the set of original confocal microscope images of cell #8 among the imaged cells is shown in Fig. 1. Analysis of the imaged cells demonstrated that a typical B-cell, when not in the dividing phase, appears to have an approximately spherical shape for its plasma membrane and nucleus. In the case of cell #8, the membrane and nucleus are also approximately concentric.

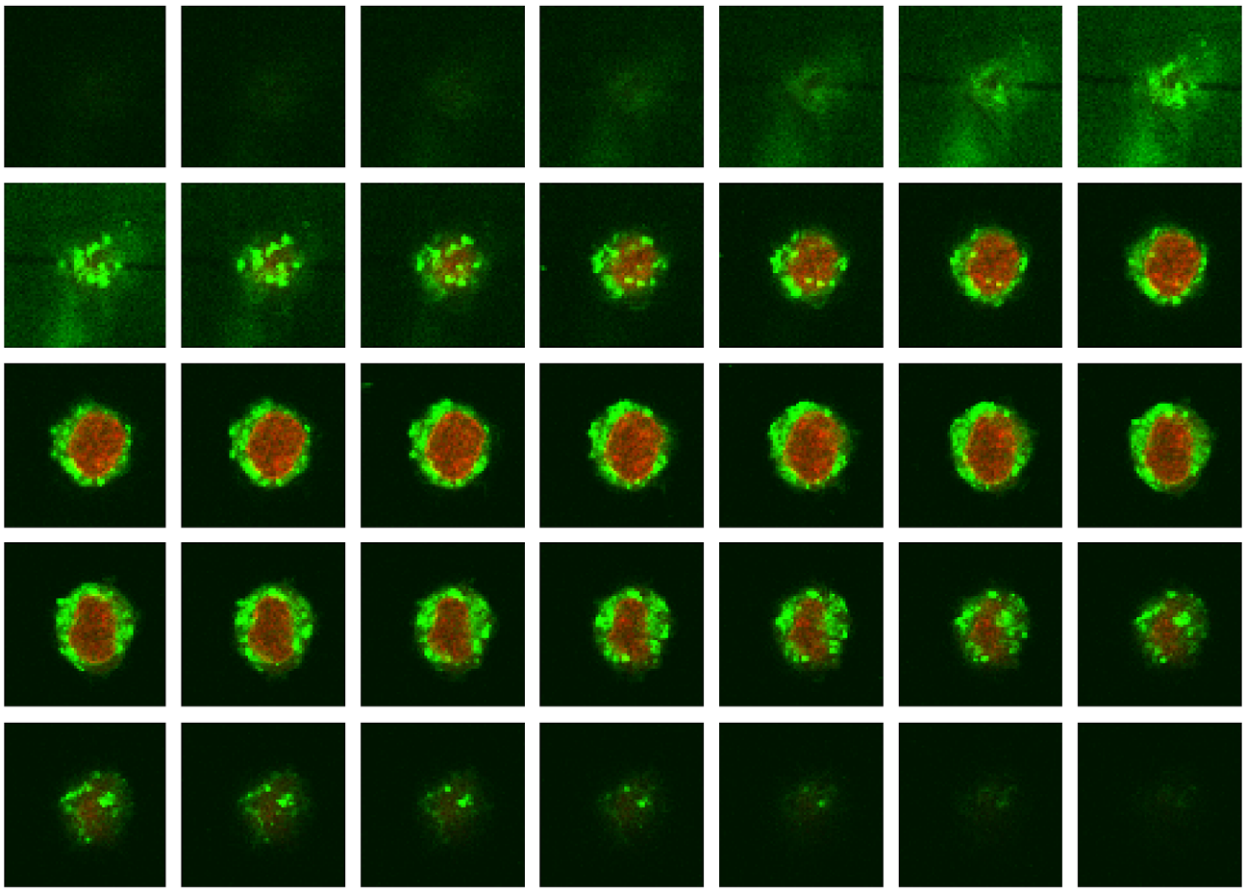

Fig. 1. The stack of 2D confocal images of a NALM-6 cell (cell #8) acquired along the z-axis through the cell. The plasma membrane is stained with green dye and the nucleus with red dye.

We have chosen cell #8 for the FDTD scattering simulations presented in this paper partly because its structure appears to be close to a coated sphere, for which an analytic solution is available for comparison. This comparison may clearly illustrate the effect of structure on light scattering.

2.2. Automated image processing

Based on the image features of the B-cells, we developed a procedure to automatically extract the border contours of the nucleus and the cell membrane, where the former is shown in red and the latter in green in a 2D confocal image. To demonstrate this procedure, image #17 in Fig. 1 is singled out to illustrate the main steps in the procedure with the original 2D image redisplayed in Fig. 2a. A quick examination of Fig. 2a shows that while the intensity distributions are not very even for both of the fluorescence colors, the dynamic range of the red fluorescence is much smaller than that of the green fluorescence for which many pixels have reached saturation readings. We first separated the two color components in the image pixels of RGB format so that the contours of the nucleus and the cell membrane can be obtained separately. As an example, the red component of Fig. 2a is presented in Fig. 2b which shows the nuclear region with a clear border line. A closer examination of Fig. 2b also shows that separation of the color components reveals some additional information that is not observable in the original image: there is a rim of weak red color around the nucleus resembling the shape of the cytoplasm, which may have been caused by a low density residue of the red dye molecules inside the cell cytoplasm. Even though the red component of the pixels in this region has a much smaller intensity readings than those in the nuclear region, it is very uniform and shows clearly the border of the cell membrane. Further investigation of the cells stained with only red or green dyes confirmed these observations. In comparison, the saturated pixels in the green intensity readings of the cytoplasm makes it very difficult to automatically extract the contour of the cell membrane accurately with the green component alone. For these reasons, only the red component of the pixels is used for the automated image processing while the green component is used only for confirmation purpose.

The image processing is started by retrieving the statistics of intensity readings. First, the geometric center of the imaged cell in 3D space is located by pooling all the pixels of the entire image stack together. Then the 2D image slide that is closest to the center is identified as the reference slide. The intensity distribution in the reference slide is obtained by sorting the intensity readings from all pixels into a histogram of the intensity readings from 0 to 255. In the case of Fig. 2b, the red component of the pixels shows three groups in its intensity reading distribution with each corresponding to a region in the image, those within the group of highest intensity reading are regarded as in the nucleus, those within the group of the lower reading are regarded as in the cytoplasm and those with readings much lower than the cytoplasm group are classified as the noise background.

The next step is to group the pixels in other 2D images by comparing their intensity readings to the ranges of the three intensity groups obtained from the reference slide in the previous step. As in the reference slide, the

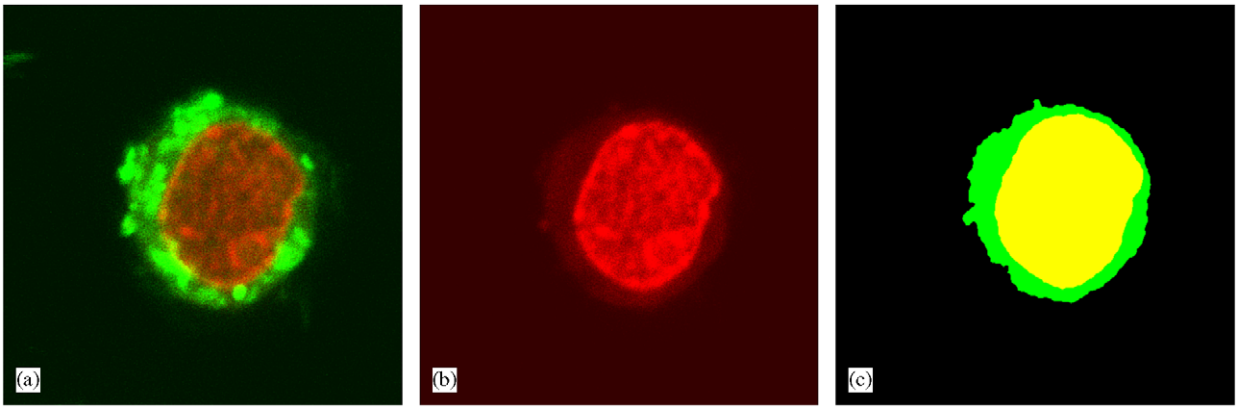

Fig. 2. Imaging processing with image #17 shown in Fig. 1 as an example: (a) original image; (b) red component after color separation; (c) processed image.

pixels are labeled as either in the nuclear group, the cytoplasm group, or the background group. The sorted pixels in each 2D image are then recombined to form a false-color copy as a processed image: pixels labeled as inside the nucleus assigned with a yellow color, those in the cytoplasm with a green color and the background pixels with black (intensity = 0). The third step is to remove the "single" specks. In this part the following rules are applied: (1) if a pixel is not assigned as a background pixel but is "surrounded" by background pixels, then it becomes a background pixel; (2) if a pixel is assigned as a background pixel but is "surrounded" by non-background pixels then it becomes a non-background pixel.

Once an image is divided into different regions or clusters with one of the two colors, yellow or green among the black background, the largest clusters of non-background pixels are determined among the pixel clusters. A cluster consists of connected pixels of the same color (yellow or green) with a size given by the number of pixels. Note that in the last step the clusters of size 1 have been removed. Ignoring the background cluster, the largest cluster in each color is chosen and considered to be the item of interest, i.e., the cytoplasm or nucleus. The pixel distributions in the false-color images are then smoothed using a method of Gaussian 2D window averaging to remove the "specks" or the pixels with intensity readings significantly different from their neighboring pixels. This was carried out via the convolution of the intensity reading of a pixel over a grid of 16×16, centered on that pixel, with a kernel of $\exp\{-(i^2+j^2)/3^2\}$ for $-8 \leqslant i \leqslant 8$ and $-8 \leqslant j \leqslant 8$. After averaging, the intensity readings of all pixels are set to either 0 or 255 if they were smaller or greater than a threshold value, respectively. This procedure was very effective to remove the specks consisting of several pixels in the image processing code.

In the last part of image processing, the stack of the false-color images generated from the confocal images is examined to eliminate those images with dominant noise background pixels. These are defined as the image slides with less than 25 non-background pixels among the 512×512 pixels and, if any, are found to be those at the top or bottom of the imaged cells. The output of the above processing procedure is a stack of false-color images containing solid areas of different colors representing the cytoplasm and the nuclear regions, as displayed by the processed image of Fig. 2b in Fig. 2c. These images provide the input data for the shape generator program.

2.3. 3D structure construction

A shape generator program has been developed to read the processed images and generate the 3D structure in the following steps.

The first step involves border extraction and parameterization in each 2D image. For each of the two colors, all interior pixels are removed to obtain the border contour lines of the cytoplasm and nucleus. Since these border lines are simple (non-self-intersecting) and closed, they can be represented by parameterized curves which are also simple and closed, i.e., the Jordan curves [17]. The parameterization is chosen such that the following is true: the border is a trace of the curve $f(t)$ with $0 \leqslant t \leqslant 1$ and $f(0) = f(1)$. The starting point of the curve, $f(0)$, is selected by locating the lowest pixel of the border intersecting with a vertical line that passes through the geometric center of the cellular component (cytoplasm or nucleus).

In the second step, the boundary surface of a cellular component in 3D space is constructed by linear interpolation between the border lines in the adjacent image slides. For cytoplasm or nucleus, the parameterized border curve in each image slide is connected by line segments to the curves on the adjacent slides along the z-axis with the same values of t. The boundary surface in the 3D space can then be constructed with these line segments through the stack of the border curves as densely as desired using a small increment of the curve parameter t. To make up the eliminated image slides near the top and bottom of the imaged cell due to the dominant noise background, the top and bottom portions of the boundary surface for the cell and nucleus are constructed by extrapolation from the slides near the two ends of the image stack.

The final step is to assign a domain ID to each FDTD grid point. Since the imaged NALM-6 cells have relatively simple structures of cytoplasm and nucleus, we assumed that the surfaces of the cell membrane and nucleus are simple and closed. This allows the separation of grid points into two groups of either "inside" or "outside" of a surface. For a particular point, the classification is determined by the number of intersections between the surface and a ray drawn from the grid point to infinity. This separation is based on the extension of the Jordan curve theorem and its corollary [17] to the 3D space. Note that the nuclear boundary takes

precedence in separating the grid points since they are within the cell membrane boundary. After the separation, each grid point is assigned one of the three domain IDs depending on whether it is in the nucleus, cytoplasm or the hosting medium outside the cell.

To study the effect of the realistic shape and structure of a B-cell on its scattering pattern, we adopted the FDTD method used in our recent red blood cell scattering studies [11,12]. A previously developed high-performance parallel FDTD code [12] was modified to import the 3D cell structure constructed in the way described above. We calculated the distribution of the scattered light in terms of the angle-resolved Mueller matrix elements for different directions of the incident light beam.

3. Results and discussions

3.1. Validation of the 3D construction procedure

It has been observed that there is a slight stretching of the 3D shape along the z-axis due to the stepping error of the sample stage in the confocal microscope. To eliminate the deformation and examine the effect of optical aberration and image construction error, we applied the construction procedure described in the last section to polystyrene spheres. Commercially available spheres of 6 μm in diameter and coated with green dye were used for this purpose. A stack of confocal images of a sphere have been acquired (in Fig. 3a) under similar conditions to those of the B-cell imaging with only one excitation laser beam at 488 nm. The shape of the sphere in the 3D space was constructed with the processed images, and the stepping error of the z-scan was determined by a best fitting factor to produce the "most spherical" shape. Two different views of the constructed sphere are presented in Fig. 3b, which clearly shows that the constructed shape is not perfectly spherical. This can be attributed to the optical aberration of the microscope as well as the error caused by the interpolation and extrapolation procedures employed in the construction procedure. The green color in Fig. 3b is an artificial color used by the viewing software (VisCAM View, Marcam Engineering GmbH) to indicate the outside of a closed surface.

To determine the effect of deviations from a spherical shape on scattering patterns, we calculated the scattering phase function or the element S_{11} of the Mueller matrix normalized over the entire range of solid scattering angle, from the constructed sphere using the FDTD method for selected angles of incidence. Due to the symmetry of the shape, three representative angles of incidence at 0°, 45°, and 90°, with 0° for light incident along the z-axis, were selected. The phase function averaged over the three angles of incidence is compared with that obtained from Mie theory of the scattering from an ideal sphere of the same volume (radius = 3 μm) in Fig. 4. For both calculations, we assumed an incident wave of wavelength $\lambda_0 = 1\,\mu\text{m}$ in vacuum, the complex refractive index of the sphere as $n_{\text{sp}} = 1.3675 + i1.0 \times 10^{-5}$ in a host medium of refractive index of $n_{\text{h}} = 1.35$. The FDTD grid cell size was set at $\Delta x = \lambda/30$ with λ as the wavelength of the incident light in the host medium. The refractive index of each region n is related to the respective dielectric constant ε by $n = \sqrt{\varepsilon}$. We also calculated the scattering cross-sections for both cases, and they were found to be very close: 45.8 μm^2 for the sphere and 47.0 μm^2 for the constructed shape averaged over the three angles of incidence

It can be seen from Fig. 4 that the results match fairly well over the full range of the scattering angle, with the results from the constructed shape showing a smaller oscillation amplitude. These results demonstrate that the overall trend in the angular distribution of the scattered light is not affected by the small shape deformation in the constructed sphere. The characteristic oscillations in the scattering phase function of a perfect sphere are the direct consequence of the spherical symmetry; therefore, this feature is very sensitive to any departure from this symmetry. The difference in the oscillation amplitudes between the two curves in Fig. 4 thus can be reasonably related to the reduced degree of spherical symmetry in the constructed shape due to the shape deformation.

On the contrary, biological cells posses very little symmetry in their structures due to non-spherical shapes, surface structures, and heterogeneity introduced by the intracellular components. It is thus reasonable to expect that the optical aberrations in imaging and construction errors observed in the case of the sphere should have much less impact on the distributions of light scattered by real cells. For example, the amplitude of the membrane roughness, in bending and folding, and other non-spherical features in the shape of

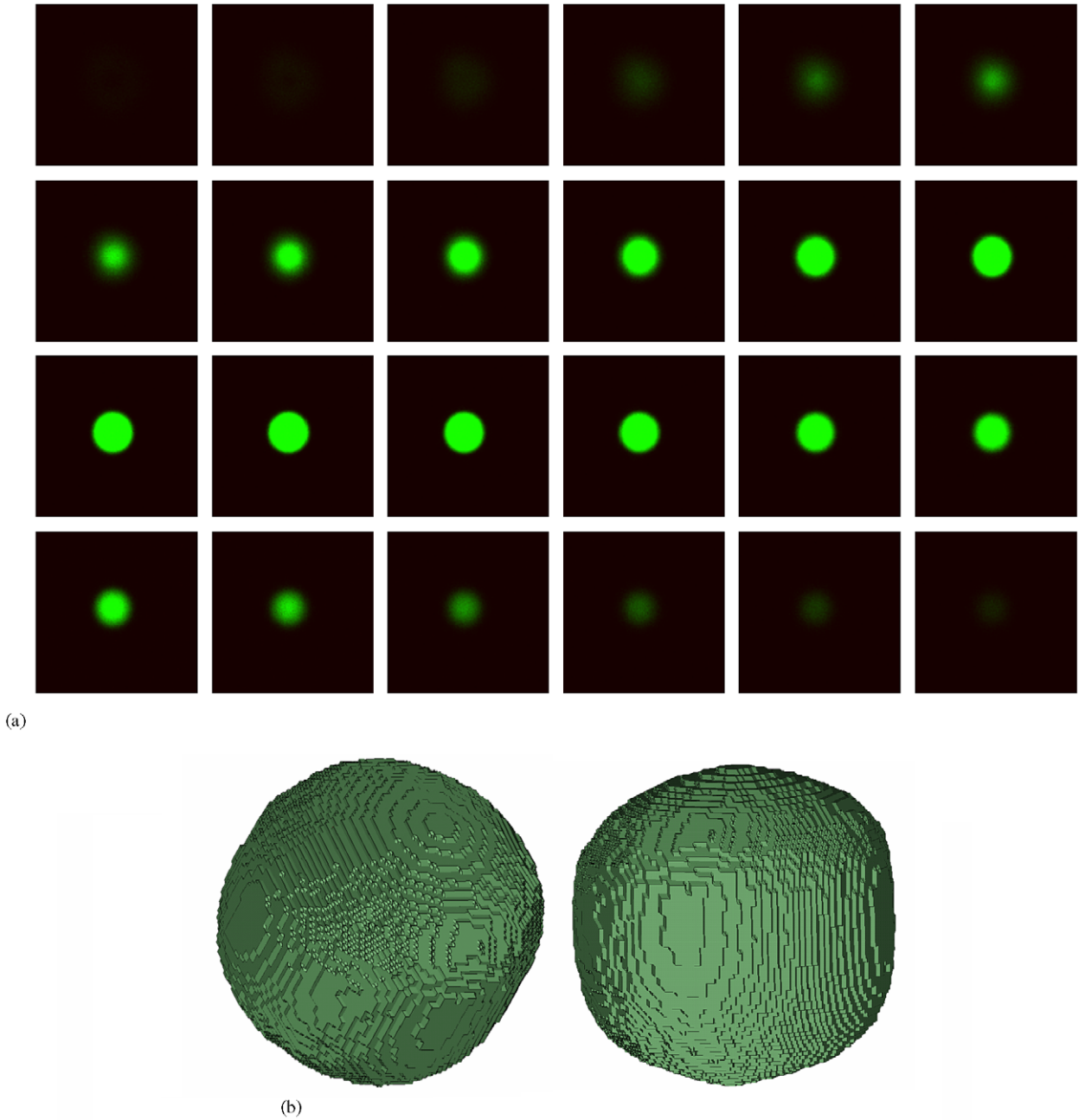

Fig. 3. 3D structure construction of a sphere of 6 μm in diameter and coated with green dye: (a) the stack of 2D confocal images; (b) two views of the constructed sphere.

malignant B-cells observed by electron microscope [13] are typically larger than the imaging and construction errors of 0.3 μm or less. Therefore, it should be much less likely in these cases that such errors will affect significantly the light scattering patterns. We should point out that further improvement over present work, which represented the first results of constructing realistic 3D structure of biological cells for optical simulations, can be achieved by refining the staining process and improving the interpolation precision.

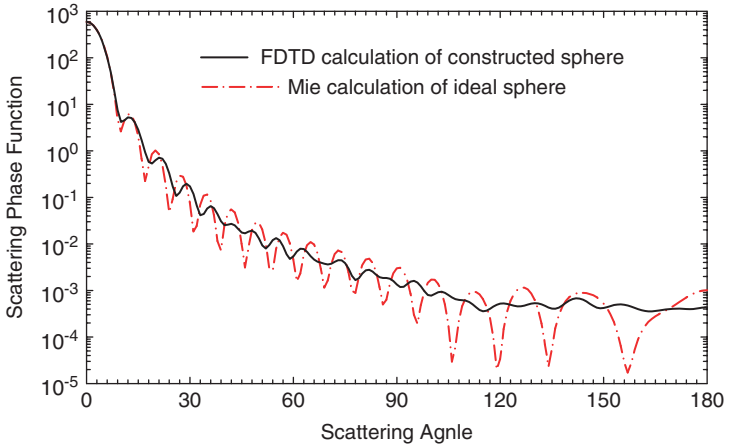

Fig. 4. The angle-resolved scattering phase function calculated by the FDTD method and averaged over 3 angles of incidences for the constructed sphere in Fig. 3 and that of an ideal sphere of same diameter calculated by Mie theory.

3.2. Light scattering simulations with the constructed B-cell structure

As a first application of the image processing procedures, we constructed the 3D structure of cell #8 from the stack of 2D confocal images presented in Fig. 1, with the external and cross-section views of the constructed cell shown in Fig. 5. It should be noted that the software, VisCAM View, used to produce the images in Fig. 5 utilizes the green and red colors artificially to label the outside and inside of a closed 3D surface, respectively. For this reason, the inside of the boundary surface appears in red and the outside in green for both nucleus and cell membrane. In obtaining the final structure, the step size along the z-axis between the image slides has been rescaled by the same factor obtained from the sphere calibration. The 3D numerical structure was then imported into the FDTD program, where the proper values of dielectric constant were assigned to each grid point according to its domain ID, indicating either inside the nucleus, cytoplasm, or the region outside the cell, to calculate the Mueller matrix elements for different orientations of the cell [11,12]. It should be noted that the 3D structure shown in Fig. 5 is plotted with a grid cell size of $0.148 \times 0.148 \times 0.148\,\mu m^3$ while the 3D structure mapped for FDTD simulations uses a finer grid cell size of $0.037 \times 0.037 \times 0.037\,\mu m^3$ to satisfy the FDTD resolution requirement. The 3D structure construction allows easy estimation of geometric properties of the imaged cell such as volume and surface area. In the case of cell #8, the nuclear volume was calculated to be $293\,\mu m^3$ and the cell volume to be $557\,\mu m^3$ with the nucleus occupying about 52% of the cell volume. Both the nucleus and the cytoplasm regions were assumed to be homogeneous with complex indices of refraction of $n_n = 1.4 + i1.0 \times 10^{-5}$ for the nucleus and $n_c = 1.3675 + i1.0 \times 10^{-5}$ for the cytoplasm at an incident wavelength $\lambda_0 = 1\,\mu m$ in vacuum [5]. It was further assumed that the cell is suspended in a transparent water-like host medium with a refractive index $n_p = 1.35$. The FDTD grid cell size was set at $\Delta x = \lambda/20$ with λ as the wavelength of the incident light in the host medium.

The angle-resolved Mueller matrix elements of the cell, in terms of the polar scattering angle θ_s and azimuthal scattering angle ϕ_s, were obtained for 30 different angles of incidence (denoted by θ_i and ϕ_i) over the full range of the solid angle [11]. Representative results for several angles of incidence revealing the major features of scattering pattern are shown in Fig. 6, where five independent Mueller matrix elements [18] of the cell that have been averaged over the azimuthal angle ϕ_s are plotted as functions of the scattering angle θ_s. Also shown in the same figure are the results averaged over all 30 angles of incidence that have been studied. It can be seen from Fig. 6 that the results obtained at different angles of incidence show similar patterns for each of the Mueller matrix elements. Curves for different angles of incidence agree with each other well in the region of the forward scattering with $\theta_s < 20^\circ$. As θ_s increases from 20° to 80° they start to differ and exhibit much less correlation for $\theta_s > 100^\circ$.

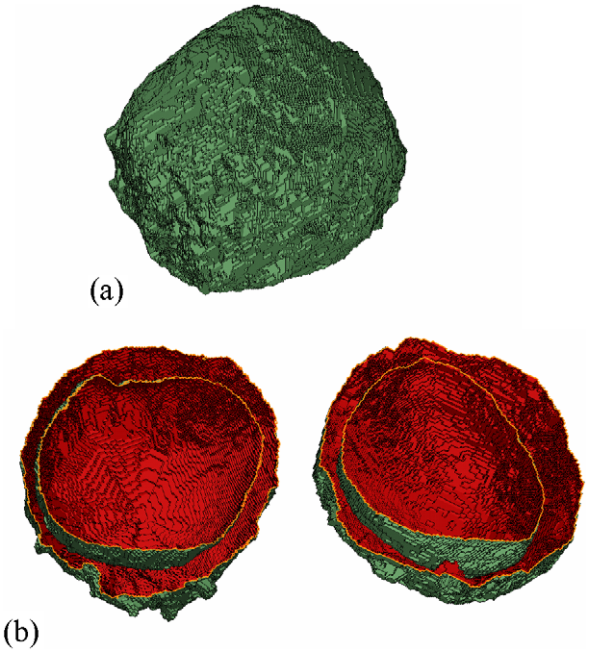

Fig. 5. Constructed 3D structure of cell #8: (a) external view; (b) two cross-section views.

Since the constructed structure of cell #8 appears to be spherical with concentric cell membrane and nucleus, we employed a coated sphere as a comparison model to study the effect of detailed structure on light scattering. Here the core of the coated sphere was set to have the same refractive index and volume of the nucleus and the shell to have those of the cytoplasm of the cell #8, yielding radii of 4.12 and 5.10 μm for the core and shell, respectively. The problem of light scattering by a coated sphere can be solved exactly and the results presented here were calculated using the code DMILAY developed by Toon and Ackerman [19]. The results of four non-trivial Mueller matrix elements for the coated sphere are compared in Fig. 7 with the incident angle averaged results of the same elements of cell #8 with the constructed structure. It should be noted that the curves of element S_{11} presented here have not been normalized, so that the overall scattering features including the scattering power, measured by the scattering cross-section, and the scattering pattern, presented by the phase function, can be compared together. It can be seen that the angle-resolved matrix elements of the coated sphere have the characteristic oscillations associated with the spherical symmetry while those of the cell #8 are much smoother due to the incidence angle averaging and lack of symmetry in structure. Overall, those two sets of results do not match very well. The disparity is particularly pronounced in the element S_{11} where the results of the coated sphere are consistently lower than those of cell #8 in the larger scattering angle region, especially for $\theta_s > 120^\circ$. This indicates that the coated sphere is a poor model for the imaged B-cell at large scattering angles; even though it appears to have a spherical structure. In the forward scattering region, however, they match almost perfectly for $\theta_s < 20^\circ$. Therefore, we can observe that the deviation of a scatterer's structure from spherical symmetry does not affect forward scattering. Combined with the results shown in Fig. 6 on the effect of incidence angle or cell orientation, we may further note that the forward scattering ($\theta_s < 20^\circ$) provides information sensitive only on the volume of the scatterer; an experimental fact noted in numerous reports on light scattering by cells [20].

To understand the marked difference between these two sets of results at large values of θ_s, we also calculated the Mueller matrix elements of an equivalent sphere to investigate the effects of scatterer volume. Here the equivalent sphere is defined to be a homogeneous sphere of the same volume as the constructed cell with an effective index of refraction obtained by averaging the indices of the nucleus and the cytoplasm weighted by their volumes. The results are also plotted in Fig. 7 for comparison with the other two sets of results. It can be seen that the results from the equivalent sphere are closer to those of the constructed cell than

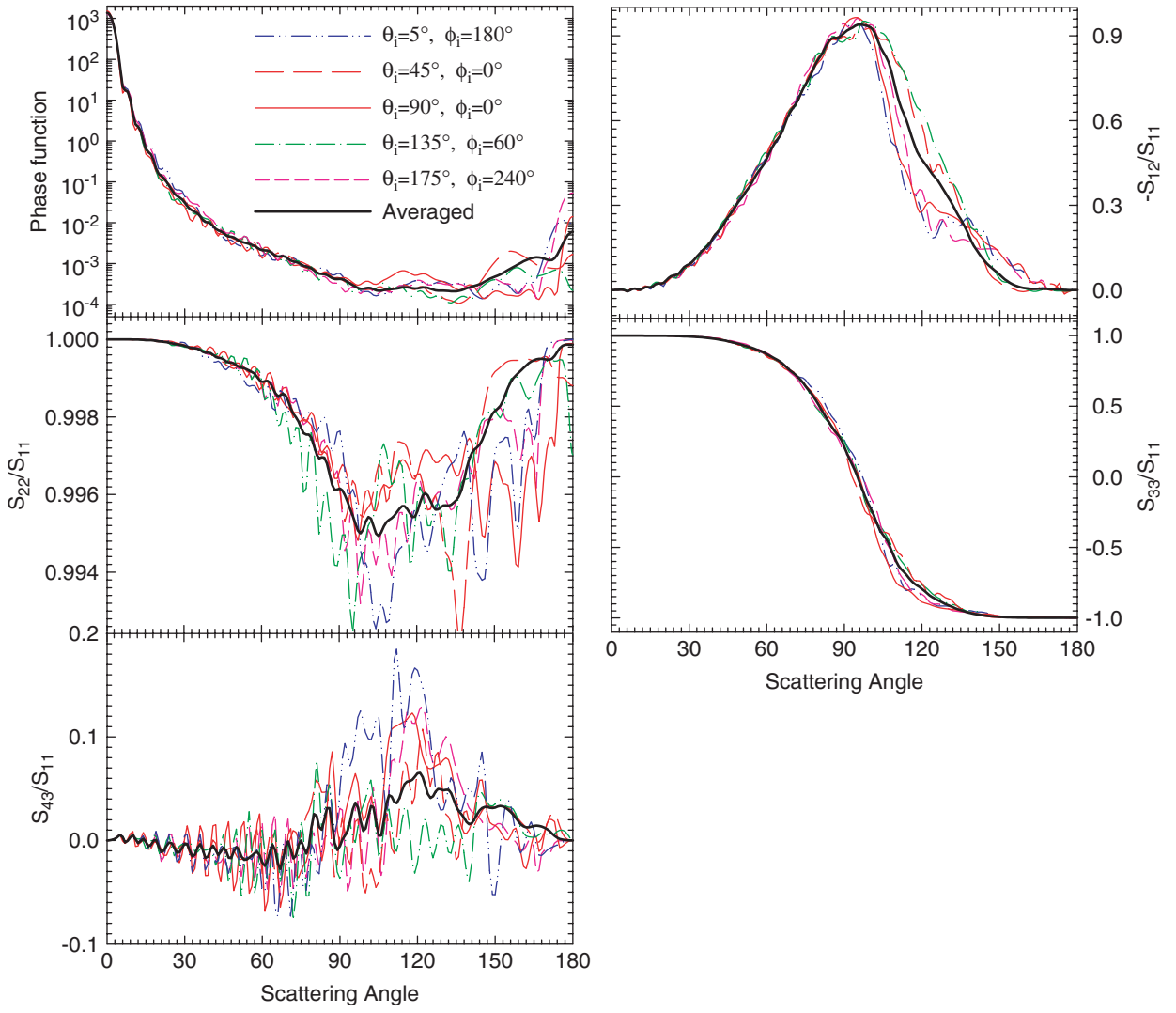

Fig. 6. Five angle-resolved Mueller matrix elements for the constructed cell #8 in Fig. 5 at representative angles of incidence. Also presented are the results averaged over 30 angles of incident for each element.

that of the coated sphere for most large scattering angles. But unlike the coated sphere, the good match with the results of the constructed B-cell near the forward direction in the S_{11} ends near $\theta_s = 5^\circ$, far short of the 20° for the coated sphere.

Based on these observations, we conclude that the forward scattering signals with $\theta_s < 5^\circ$ provide accurate information on the volume of the scatterer. The agreement between the results of the coated sphere and the constructed B-cell in the region of $5^\circ < \theta_s < 20^\circ$ demonstrates that additional structural elements should be added to improve the accuracy of sphere modeling of light scattering by B-cells with structures close to coated spheres. The marked difference between the sphere models and the constructed cell #8, which is a simplified copy of the real B-cells, over the regions of $\theta_s > 20^\circ$ indicates that the detailed structural features in the B-cell affect significantly the side- and back-scattered light signals. This conclusion is supported by the results of our previous FDTD studies of light scattering from red blood cells of different shapes [11,12]. It has been shown there that the variation in the large-scale structural features can result in changes in light scattering pattern at most scattering angles, while the small-scale distortions can produce significant changes in the scattering

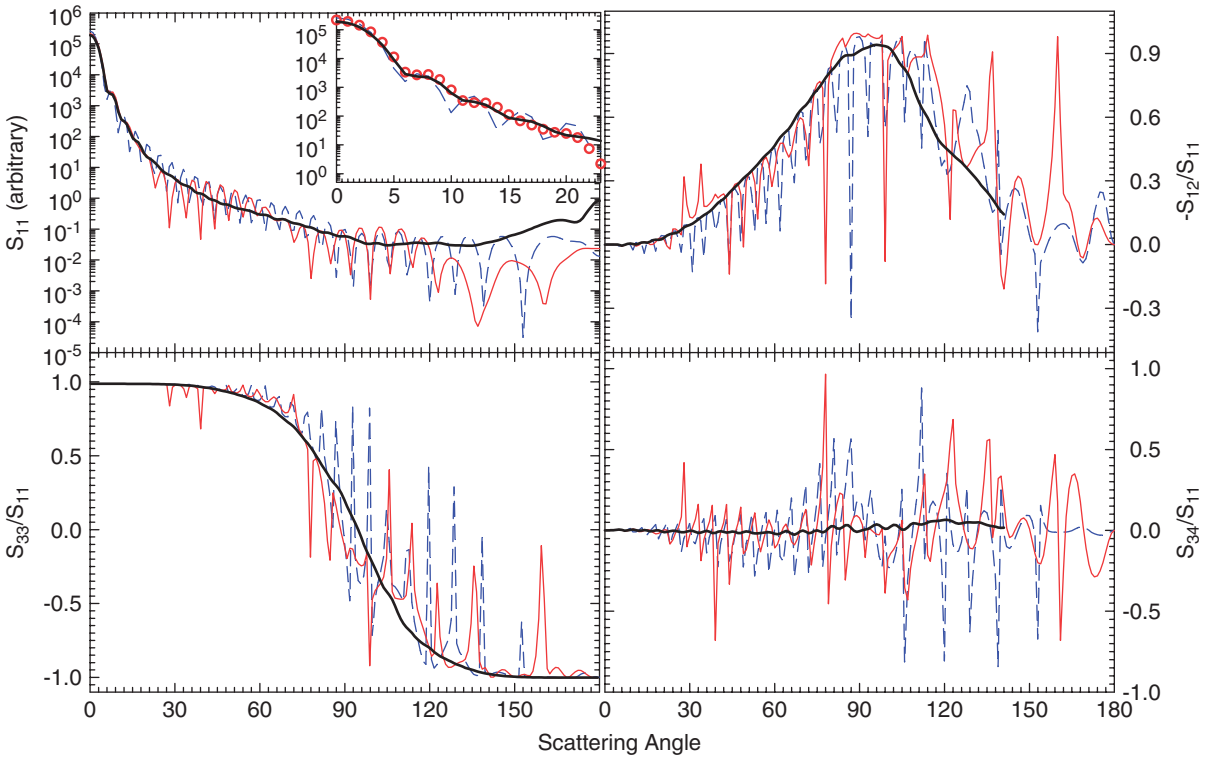

Fig. 7. Comparison of angle-resolved Mueller matrix elements: FDTD results with incident angle averaging for the constructed cell #8 (thick solid lines); Mie results for coated sphere (solid lines) and effective sphere (dash lines). The inset in the plot of S_{11} shows the three curves for small angles with the coated sphere results represented by the open circles for better visibility.

pattern in the backscattering region. And those changes are most evident in the region of $\theta_s > 90^\circ$ when certain symmetry of the structure is involved.

4. Summary

To investigate the effect of realistic structure on the light scattered by a biological cell, we have developed an automated procedure to construct the 3D structure of a NALM-6 cell from its confocal images. A parallel FDTD program was applied to calculate selected Mueller matrix elements of the constructed structure. The FDTD simulation results with the constructed cell structure have been compared to those of sphere models to provide insight on the effect of detailed cellular structures on light scattering. Even though the shapes of the membrane and the nucleus of the constructed B-cell appear approximately spherical and concentric, a coated sphere was shown to be a poor model for the study of light scattering at large scattering angles. On the other hand, the good agreement between the results from the coated sphere model and the constructed B-cell for $\theta_s < 20^\circ$ indicates that the sphere model may be used for phase function estimation in the forward scattering region.

Acknowledgments

XH and JQL would like to express their gratitude to Prof. A. P. Bode at the Department of Pathology and Laboratory Science of East Carolina University (ECU) for suggesting the use of B-cells for their light scattering study. The cultured NALM-6 cells were generously provided by Prof. F. E. Bertrand at the Department of Microbiology and Immunology of ECU. This work was supported in part by a NIH Grant (1R15GM70798-01) and by NPACI through supercomputer time allocations.

References

[1] Wyatt PJ, Phillips DT. Structure of single bacteria from light scattering. J Theor Biol 1972;37:493–501.
[2] Bickel WS, Davidson JF, Huffman DR, Kilkson R. Application of polarization effects in light scattering: a new biophysical tool. Proc Natl Acad Sci USA 1976;73:486–90.
[3] Bickel WS, Stafford ME. Polarized light scattering from biological systems: a technique for cell differentiation. J Biol Phys 1981;9:53–66.
[4] Volten H, de Haan JF, Hovenier JW, Schreus R, Vassen W, Dekker AG, et al. Laboratory measurements of angular distributions of light scattered by phytoplankton and silt. Lumnol Oceanogr 1998;43:1180–97.
[5] Mourant JR, Canpolat M, Brocker C, Esponda-Ramos O, Johnson TM, Matanock A, et al. Light scattering from cells: the contribution of the nucleus and the effects of proliferative status. J Biomed Opt 2000;5:131–7.
[6] Yurkin MA, Semyanov KA, Tarasov PA, Chernyshev AV, Hoekstra AG, Maltsev VP. Experimental and theoretical study of light scattering by individual mature red blood cells by use of scanning flow cytometry and a discrete dipole approximation. Appl Opt 2005;44:5249–56.
[7] Salzman GC, Singham SB, Johnston RG, Bohren CF. Light scattering and cytometry. In: Melamed MR, Lindmo T, Mendelsohn ML, editors. Flow cytometry and sorting. 2nd ed. New York: Wiley; 1990 [chapter 5].
[8] Maltsev VP. Scanning flow cytometry for individual particle analysis. Rev Sci Instruments 2000;71:243–55.
[9] Dunn A, Richard-Kortum R. Three-dimensional computation of light scattering from cells. IEEE J. Selected Top Quantum Electron. 1996;2:898–905.
[10] Drezek R, Guillaud M, Collier T, Boiko I, Malpica A, Macaulay C, et al. Light scattering from cervical cells throughout neoplastic progression: influence of nuclear morphology, DNA content, and chromatin texture. J Biomed Opt 2003;8:7–16.
[11] Lu JQ, Yang P, Hu XH. Simulations of light scattering from a biconcave red blood cell using the FDTD method. J Biomed Opt 2005;10:024022.
[12] Brock RS, Hu XH, Yang P, Lu JQ. Evaluation of a parallel FDTD code and application to modeling of light scattering by deformed red blood cells. Opt Express 2005;13:5279–92.
[13] Terzakis JA. Distinguishing B and T lymphocytes by scanning electron microscopy. Ultrastruct Pathol 2000;24:205–9.
[14] Taflove A, Hagness SC. Computational electrodynamics: the finite-difference time-domain method, 2nd ed. Boston, MA: Artech House; 2000.
[15] Yang P, Liou KN. Finite difference time domain method for light scattering by nonspherical and inhomogeneous particles. In: Mishchenko MI, Hovenier JW, Travis LD, editors. Light scattering by nonspherical. Travis, San Diego: Academic Press; 1999 [chapter 7].
[16] Hurwitz HR, Hozier J, LeBien T, Minowada J, Gajl-Peczalska K, Kubonishi I, et al. Characterization of a leukemic cell line of the pre-B phenotype. Int J Cancer 1979;23:174–80.
[17] O'Rourke J. Computational geometry in C, 2nd ed. Cambridge, New York: Cambridge University Press; 1998.
[18] Hovenier JW, van de Hulst HC, van der Mee CVM. Conditions for the elements of the scattering matrix. Astron Astrophys 1986;157:301–10.
[19] Toon OB, Ackerman TP. Algorithms for the calculation of scattering by stratified spheres. Appl Opt 1981;20:3657–60.
[20] Melamed MR, Lindmo T, Mendelsohn ML. Flow cytometry and sorting, 2nd ed. Wiley-Liss: New York; 1990.